

Application and Parameterization of a 1D Multifluid Population Balance Model to Bubble Columns

Ferdinand Breit¹, Christian Weibel¹, and Erik von Harbou¹

¹Rheinland-Pfälzische Technische Universität Kaiserslautern-Landau

November 16, 2023

Abstract

A 1D multifluid population balance model approach is presented as a compromise between computational effort and accuracy. The approach is used to test process scenarios, perform sensitivity analysis, and provide a reliable scale-up and optimization tool. The study focuses on a mini-plant batch bubble column, where the scale-up behavior in terms of bubble column height, gas flux, and composition of the liquid phase is investigated. Although simplifications were made, the model requires calibration to experimental data using different calibration methods. An optimal calibration procedure is found that minimizes experimental effort while maximizing scalability. The model was tested on various liquid-phase compositions, and it was found to reproduce experimental data accurately. However, the model cannot reproduce flow regime changes and does not perform well outside the calibrated concentration. The study shows that the applied 1D multifluid populations balance approach is a valuable and reliable tool in multiphase reactor scale-up and optimization.

Application and Parameterization of a 1D Multifluid Population Balance Model to Bubble Columns

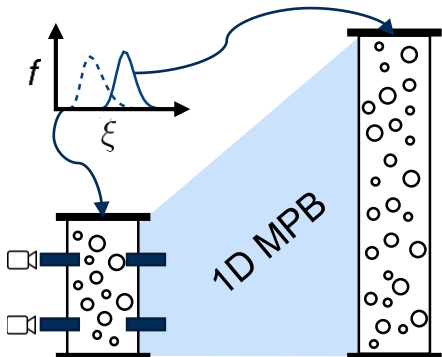
Ferdinand Breit¹, Christian Weibel¹ and Erik von Harbou¹

¹Laboratory of Reaction and Fluid Process Engineering, University of Kaiserslautern-Landau, Gottlieb-Daimler-Straße 44, 67663 Kaiserslautern, Germany

Abstract

A 1D multifluid population balance model approach is presented as a compromise between computational effort and accuracy. The approach is used to test process scenarios, perform sensitivity analysis, and provide a reliable reactor scale-up and optimization tool. The study focuses on a mini-plant batch bubble column, where the scale-up behavior in terms of bubble column height, gas flux, and composition of the liquid phase is investigated. Although simplifications were made, the model requires calibration to experimental data using different calibration methods. An optimal calibration procedure is found that minimizes experimental effort while maximizing scalability. The model was tested on various liquid-phase compositions, and it was found to reproduce experimental data accurately. However, the model cannot reproduce flow regime changes and does not perform well outside the calibrated concentration. The study shows that the applied 1D multifluid populations balance approach is a valuable and reliable tool in multiphase reactor scale-up and optimization.

Graphical Abstract



1 Introduction

Many industrially important syntheses involve reactive multiphase systems [1, 2]. Examples are homogeneously or heterogeneously catalyzed oxidation, hydrogenation, carboxylation or hydroformylation reactions. In order to scale up these processes from laboratory to production scale and to design the required reactor vessels, the engineer needs insight into the influence of process conditions (e.g. temperature, pressure, power input), system properties (e.g. reaction rate, gas solubility) and reactor geometry (e.g. vessel height and diameter, geometry of internals) on the behavior of the multiphase process (e.g. space-time yield achieved). In many cases, these insights into the complex interactions cannot be obtained by experiments alone, mostly because of the multitude of parameter combinations and the difference in scale between laboratory and production (e.g. ratio of shell area to volume, ratio of bubble size to reactor diameter). Thus, models are required that can describe these interactions reliably in a large parameter range. The engineer can use these models to find the optimal reactor design for a given synthesis task or to predict the behavior of a given reactor under varying process conditions.

Our recent study on the behavior of gas-liquid jet loop reactor [3] illustrates well the complex interactions that can occur in reactive multiphase systems. By means of a model, we were able to show that the consumption of gas caused by a reaction in the liquid phase can influence the internal circulation flow of the jet loop reactors significantly. This behavior

could be attributed to local differences in the gas volume fraction. The model prediction enables the identification of critical ranges of both process and geometry parameters in which the gas consumption can lead to a complete break-down of the internal circulation flow. Thus, this study shows the complex interactions of different parameters in reactive multiphase processes and the importance of models that can describe the behavior of these processes. Many other studies and model approaches can be found in the literature which underline this fact. [4–6].

Even though our model presented in [3] proved to be very useful to gain a better understanding of the behavior of the jet loop reactor, it is far from covering all phenomena that can influence the internal circulation flow and the gas consumption (i.e. the reaction). In fact, many complex interactions of different processes and properties as shown in Fig. 1 can be relevant for the general behavior of reactive multiphase systems and must be principally considered in the model. To give an example, the variations of the local gas volume fraction in the jet loop reactor discussed above cannot only be caused by reaction but also by local variation of the bubble rising velocity. The bubble rising velocity is directly dependent on the bubble size and therefore strongly influenced by coalescence and breakage of the bubbles. In addition, both the bubble rising velocity and the bubble size influences the interfacial mass and heat transfer and thereby they have an effect on the local gas consumption by reaction.

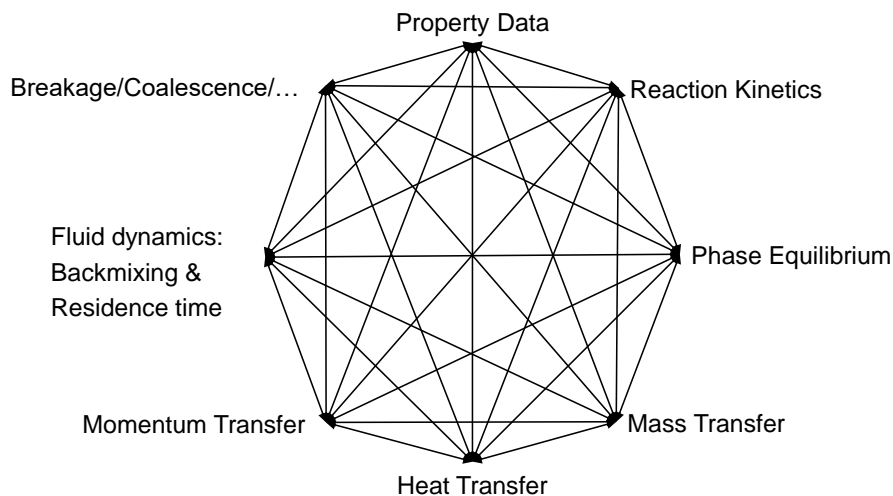


Figure 1: Illustration of reactive multiphase flow interactions.

In principle, all processes and properties presented in Fig. 1 are generally understood and can be described by models. Multiphase computational fluid dynamics (CFD) methods exist that combine these models. Thus, CFD methods can potentially provide the required detailed insights into the complex behavior of reactive multiphase processes [7, 8]. Their computational and time requirements, however, are still high [9, 10]. Thus, comprehensive studies of process and design parameters as they are often needed by the engineers in early stages of process development, are often not feasible with these methods. Moreover, predicting the exact behavior of the apparatus with high temporal and spacial resolution is often not the primary interest of the engineer. Instead, the general trends concerning the interaction of properties of the system, the process conditions and reactor geometry must be represented in order to identify unfavorable operating windows or reactor designs or to support the interpretation of observations of real production processes.

Thus, we aim at a modeling approach that takes into account the interactions of the different processes taking place in multiphase systems, and thus can reliably describe their general behavior, yet is computationally inexpensive to enable large parameter studies.

A well-proven approach to consider the properties of disperse phases in multiphase flows are population balance models. Many reports can be found in the literature in which one-dimensional (1D) – in space or time – population balance models are used to describe the size distribution of the dispersed phase in bubble columns, extraction columns, or crystallisers, see e.g. [11–22]. Recently, we applied successfully an 1D multifluid population balance approach to describe the axial profiles of gas volume fraction, the bubble size distribution (BSD) and gas phase velocity in a semi-batch bubble column operated with water and air [23]. Our 1D multifluid population balance approach (MPB) reduces the physical space $(x, y, z)^T$ to 1D (z) along the main flow direction. To describe the complex behavior of the dispersed phases namely breakage, coalescence, nucleation and growth as well as the dependency of the velocity of the bubbles on their size we applied the kinetic gas theory with size resolution (KTAWSR). This approach was developed by Jakobsen and co-workers [24, 25]. They derived new transport equations (mass, energy, momentum) for the dispersed phase that depend, like the population balance equation (PBE), also on the

property space (e.g. size of the particles). In our case, we used the KTAWSR approach to account for the transport of momentum of the gas phase so that the velocity of the bubbles becomes a function of their size.

Alternative to the KTAWSR, the common inhomogeneous MUSIG approach [26], which introduces dispersed phase velocity classes, is also suitable to describe the size dependence of the dispersed phase velocity. However, if the complex interactions as shown in Fig. 1 (e.g. the interaction between consumption of gas by a liquid-phase reaction and local velocity of phases) are to be considered, further classes in the sense of the inhomogeneous MUSIG (e.g. composition and temperature classes) would have to be introduced. Alternatively, the composition and the temperature of the dispersed phase are introduced into the PBE as additional dimensions in property space [17, 20, 21]. When considering multicomponent reactions and separation processes in future work, the number of classes and the dimension of PBE would become very large. It is expected that this high dimension of the property space or the high number of classes will be numerically very demanding. As mentioned above, KTAWSR enables to consider, in addition to the population balances, the energy, mass (total and/or species) and momentum balances for all phases. Thus, not only the velocity of the dispersed phase, but also the temperature and composition of the dispersed phase become functions of the particle size [24, 25]. However, KTAWSR has the advantage that it requires the introduction of only one additional dimension - size - instead of many classes. For this reason, we chose the KTAWSR approach for our work as a compromise between accuracy and computational complexity.

As mentioned above, we applied the MPB based on the KATSWR approach successfully to describe the velocity and size distribution in a bubble column [23]. However, since the physical space is reduced to the axial dimension (1D), local information about turbulence or back-mixing cannot be calculated directly by the model. Instead, they must be estimated from integral properties such as inlet gas flux. But local information on the turbulence and the BSD are required in the model to calculate local values for breakage and coalescence of bubbles. Therefore, due to the strong simplifications and the assumptions made, our model was not able to predict the properties of the dispersed phase correctly

when all model parameters were adopted directly from literature [23]. However, good agreement between model predictions and experiments was obtained when only a few parameters (four) of the models describing coalescence and breakage of bubbles were fitted to the measurement of local BSD in the bubble column. Obviously, the fitted parameters lump all the specific information of the process (e.g. turbulence) and the chemical system. Thus, our approach makes it possible to describe the complex behavior of dispersed phases in multiphase processes with little computational effort.

So far, the model approach has only been used to describe the bubble column process for a few variations of process conditions (superficial gas velocity) [23]. Therefore, no reliable statements can be made about the ability of the model to predict the process reliably over a wide range of parameters. In particular, it is important to know whether the model can predict process conditions outside the parameter range for which the model was trained. Therefore, in this work we present a comprehensive study of the influence of process conditions, system properties and reactor geometry on the BSD and integral gas holdup. For this purpose, the superficial gas velocity, the column height and the composition of the liquid phase were systematically varied. The composition of the continuous liquid phase was altered by using different concentrated aqueous (aq.) solutions of sodium chloride, sodium sulfite, ethanol and glycerol. The BSD was measured at 3-11 different vertical positions along the bubble column using an optical imaging probe. The optical imaging probe had been developed in-house [27]. In total, about 600 data sets including BSD and gas holdup were measured in this study. To the best of our knowledge, this is the first time that such a comprehensive database of bubble column behavior has been presented in the literature.

In order to find an optimal compromise between experimental effort (size of the training data set) and prediction performance of the model (that is the accuracy of the model prediction for both the training and validation data), a cross-validation was performed. During this cross-validation, different calibration methods, which differ in their training data set, were compared in a structured hierarchical manner, evaluated using the data of the water + air system. The resulting optimized calibration method was then applied

to the water + air system to investigate in detail the model prediction with respect to variations in column height and gas flux. As the model is to be used for reactive processes in the future, it is necessary to ensure that the accuracy of the model predictions is not sensitive to changes in property data caused by concentration changes due to reaction or mass transfer. For this study, we applied the optimized calibration method to a single composition for a given chemical system. We then examined the extent to which the model can be extrapolated to describe other compositions in that chemical system.

The results show that the model, calibrated with only two BSDs at a single vertical height, can be used to interpolate and extrapolate bubble column behavior over a wide range of gas flux, column height, measurement position, and compositions within a given chemical system.

Furthermore, we demonstrate the usefulness of the presented model approach in two exemplary studies. In these tests, the influence of process conditions and different designs on important local properties of the dispersed flow, such as the interfacial area density, are investigated. The results show that the model approach, thanks to a good compromise between the accuracy of the model predictions and the computational effort required to solve the model equations, is a perfect tool for simulation studies of multiphase systems. It provides new insights into the complex behavior of multiphase processes.

2 Experimental Setup

Fig. 2 depicts the experimental setup used in this work. This setup is based on the design applied in the work by Breit et al. [23] but without the air saturator. The primary function of the saturator was to ensure complete saturation of the air with water, thereby minimizing the interfacial mass transfer of water from the liquid phase into the gas bubbles. However, both experimental data and simulation results indicated that the saturator had no significant effect on the system behavior. The following sections provide a brief description of the experimental setup and measurement methodology. Detailed information are available in the source publication [23].

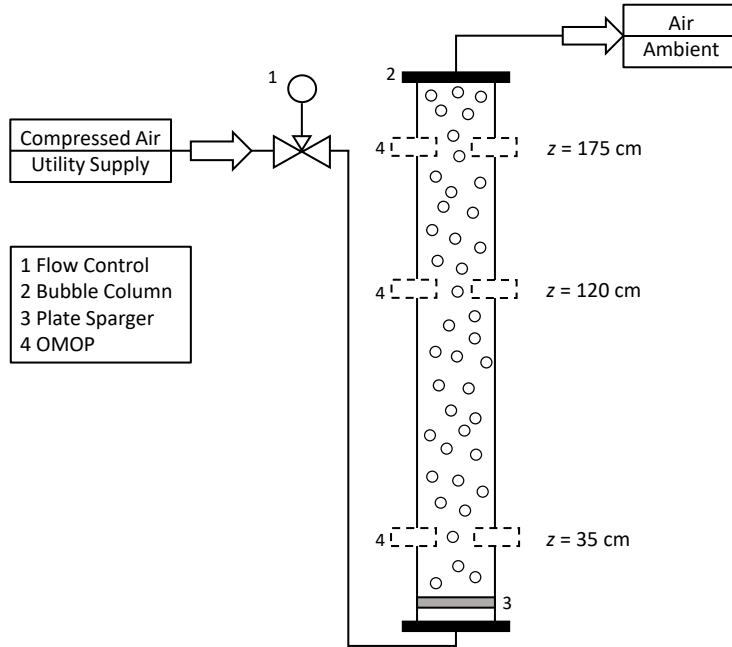


Figure 2: Schematic illustration of the experimental setup. More details are given by [23].

Compressed air from the utility supply was introduced into a Polymethylmethacrylat (PMMA) bubble column (BC) (2, the number refer to Fig. 2) through a plate sparger (3) with 163 holes of diameter 0.4 mm and a triangular hole pitch of 7.0 mm at $z = 0$ m. The inner diameter of the BC was $d_{\text{BC}} = 0.1$ m. The gas flux j_{d} was regulated by a Brooks Instrument (Hatfield, Pennsylvania, USA) mass flow controller (1) of type GF040 (GF040CXXC-0008030L-N2AVS5-XXXXXX-00C). The air passes through the liquid phase of the column before it leaves the column at the upper end ($z = z_{\text{max}}$) into the environment. The BC was filled before starting the gas flow to a height of h_c , which corresponds to the ungasified liquid height, with osmosis water (conductivity about 0.01 mS cm^{-1}), in the following just called water, or different concentrated aqueous solutions of sodium chloride (NaCl), ethanol (EtOH), glycerol (Gly) or sodium sulfite (Na₂SO₃). Note, that the aqueous solution of sodium sulfite reacts with air. However, the uncatalyzed reaction is negligible [28]. The ungasified liquid height corresponds to the BC height and is used synonymously in the following. The BSD and the gas holdup were measured for different measuring heights (just for the BSD), gas fluxes, BC heights and compositions of aqueous solutions (summary of performed experiments, see Supplementary Tab. S.1). All measurements were carried out at ambient conditions ($T^0 \approx 293$ K,

$p^0 \approx 1.0 \times 10^5$ Pa).

To determine the gas holdup, either the method of Mühlbauer et al. [29] was used or the gasified height was repeatedly read from a scale attached to the outside of the column. In both cases, the relative measurement error is estimated to be less than 1 % based on the standard deviation. Therefore, the error is not indicated in the following figures.

The in-house developed optical multimode online probe (OMOP) (4) was used to determine the BSD. It records telecentric shadowgraph images of the bubbly flow in a measuring gap (typical values are 12 mm or minimum two times the maximum bubble size). Then, an automatic algorithm detects and evaluates the bubbles so that the BSD can be calculated. Details of the setup and evaluation can be found elsewhere [27, 30]. In comparison to other image based optical measurement methods, the OMOP is characterized by its high degree of automatization for the analysis method and high number of bubbles (several thousand to ten thousand) used to calculate the BSD.

As maximal accuracy 6.4 % is specified according to Schulz, Schäfer, Bart [31] for micrometer-range particles. Therefore, we estimate an error of less than 1.0 % for particles in the millimeter range as they were found in the experiments of this work. From own repetition measurements, it is known that the percentage standard deviation of a single operation point (water + air, $z = 80$ cm, $h_c = 1.0$ m, $j_d = 4.0 \text{ cm s}^{-1}$) is about 1 % for the Sauter mean diameter and about 4 % for the variance [32]. Besagni, Inzoli [33] use a similar analysis method and specify an error of 10 % - 15 %. The OMOP should also be in this order of magnitude, tending to be better due to the used telecentric lenses and the computer-aided evaluation. A detailed investigation of the measurement accuracy is still pending. However, the existing uncertainty in the measurement error does not influence the general results and statements of this work. All of the recorded and used experimental data are summarized in [32] and are available to the public.

3 Modeling and Simulation

3.1 Governing Equations

In this work, the KTAWSR approach is applied for the balance of momentum and mass of the gas phase so that the velocity and mass of the dispersed phase (here: bubbles) becomes a function of the bubble diameter. To simplify the complex model, the following key assumptions are made:

- only the momentum and mass balance of both liquid and gas phase are considered,
- one physical space dimension along main flow direction (the column height, in the following just z -direction),
- stationary process,
- no mass transfer between phases.

In addition to the assumptions made by Breit et al. [23], the viscous effects and the influence of the virtual added mass force are neglected because their influence on the simulation results was found to be negligible. Furthermore, these simplifications lead to a significant speed-up of the simulation runs. The Eq. (1)-Eq. (4), adopted from [23–25], summarize the governing equations of the applied model.

Population balance equation of gas phase:

$$\begin{aligned} \frac{\partial}{\partial z} (f_d^m(z, \xi) u_d(z, \xi)) + \frac{\partial}{\partial \xi} (f_d^m(z, \xi) \dot{\xi}(z, \xi)) \\ = -B_D(z, \xi) + B_B(z, \xi) - C_D(z, \xi) + C_B(z, \xi) \end{aligned} \quad (1)$$

Momentum balance of gas phase:

$$\begin{aligned} u_d(z, \xi) f_d^m(z, \xi) \frac{\partial u_d(z, \xi)}{\partial z} + \dot{\xi}(z, \xi) f_d^m(z, \xi) \frac{\partial u_d(z, \xi)}{\partial \xi} \\ = -\frac{f_d^m(z, \xi)}{\rho_d(z)} \frac{\partial p(z)}{\partial z} - f_d^m(z, \xi) g + m_d(z, \xi) \end{aligned} \quad (2)$$

Mass balance of liquid phase:

$$\alpha_c(z)\rho_c \frac{\partial u_c(z)}{\partial z} + u_c(z)\rho_c \frac{\partial \alpha_c(z)}{\partial z} = 0 \quad (3)$$

Momentum balance of liquid phase:

$$\alpha_c(z)\rho_c u_c \frac{\partial u_c(z)}{\partial z} = -\alpha_c(z) \frac{\partial p(z)}{\partial z} - \alpha_c(z)\rho_c g + M_c(z) \quad (4)$$

Here $f_d^m(z, \xi)$ is the mass density function, z is the vertical position in the bubble column, ξ is the bubble diameter, and $u_d(z, \xi)$ and $u_c(z)$ is the velocity of the dispersed phase, and of the continuous phase, respectively. $\dot{\xi}(z, \xi)$ describes the growth rate in the property space ξ . $B_D(z, \xi), B_B(z, \xi)$ are sink and source with respect to bubble breakage, $C_D(z, \xi), C_B(z, \xi)$ are sink and source with respect to bubble coalescence. $\rho_k(z)$ is the mass density of phase k , (with dispersed phase: d, continuous phase: c), $p(z)$ the pressure, g gravitational acceleration constant, $m_d(z, \xi)$ momentum transfer per bubble diameter from the continuous phase, α_k the volume fraction of phase k , $M_c(z)$ interfacial momentum transfer to the continuous liquid phase.

Note, that the PBE given in Eq. (1) replaces the mass balance for the dispersed gas phase and that the volume fraction constrain see Eq. (S.9) is used to close the system of equations. The necessary boundary conditions and constitutive equations, including the equations for the estimation of the mixture properties, are summarized in Section S.2 in the Supplementary. The breakage and coalescence kernel are calculated with the model of Coulaloglou, Tavlarides [34]. This model proved to be a good compromise between accuracy and speed. The turbulent energy dissipation rate is estimated from the superficial velocity of the dispersed phase as suggested by [35].

As boundary conditions for the mass density function, the experimental BSD [32] is used directly. The property data of pure water and air as well as the parameters used to calculate the property data of the aqueous solutions are summarized in Tab. S.2 and Tab. S.3 in the Supplementary. The boundary conditions applied and further model parameters are listed in Tab. S.3 and Tab. S.4 in the Supplementary.

3.2 Method of Solution

The Eq. (1)-Eq. (4) are discretized using the orthogonal collocation method as presented in [36]. This discretization leads to a set of nonlinear equations per balance equation, which are solved separately using the Picard iteration method. In addition, the entire system of equations is solved simultaneously using the Picard algorithm. During each Picard iteration of the entire system, the grid is updated to correspond to the height of the bubble column calculated from the total liquid phase mass balance. This allows us to predict the gas holdup. See [23] for more information

3.3 Regression Model

To calibrate the model, the following regression approach is used. The independent variables \vec{X} are the gas flux j_d , the ungasified liquid height h_c , the measurement position z , the solute concentration c_s and the solute s . The dependent variables \vec{Y} are the bubble size distribution \hat{f}_d^n , moments of bubble size distribution ξ_{32}, σ, ω (see. Eq. (S.44) together with Tab. S.5) and the gas holdup $\bar{\alpha}_d$ (see Eq. (S.10)). The unknown parameters $\vec{\beta}$ are the empirical parameters C_1 to C_4 of the breakage and coalescence kernel of Coulaloglou, Tavlarides [34]. After a preliminary study, it was found that the parameter C_2 is not significant and has a large confidence interval. Thus, this parameter is set to the value $C_2 = 1.0$. In order to determine the parameters $\vec{\beta} = (C_1, C_3, C_4)$ of the model function f_{model} the minimization problem Eq. (5) is solved using the function `lsqnonline` with the trust-region-reflective algorithm provided in the Optimization Toolbox of the software MATLAB® Version R2019a (9.6.0.1072779) from the publisher The MathWorks Inc. (Natick, Massachusetts, USA). The sum of the squared absolute percentage error is used as loss function, f_{loss} .

$$\min_{\vec{\beta}} f_{\text{loss}}(\vec{\beta}, \vec{X}, \vec{Y}) = \min_{\vec{\beta}} \left(\sum_i \left| \frac{\vec{Y}_i - f_{\text{model}}(\vec{\beta}, \vec{X}_i)}{\vec{Y}_i} \right|^2 \right) \quad (5)$$

Here is i a unique identifier for an experiment characterized by the values of \vec{X}_i . A detailed preliminary investigation with the Global Optimization Toolbox of MATLAB® shows that it can be assumed that there is only one global minimum. The following values were used as initial guess for the parameter estimation: $C_1 = 0.0203$, $C_3 = 0.697$, $C_4 = 5.63$. The values were adopted from our previous work [23].

The termination condition during the calculation of the Picard iteration on the entire system and the one for the solution of the PBE (cf. Section 3.3 [23]) were reduced to $\epsilon = 1 \times 10^{-4}$ in order to save computing resources. In a preliminary study, the reduction of the termination condition did not have a significant effect on the subsequent fit result. The calibrated parameters of the different simulations can be found in the Supplementary.

3.3.1 Model Validation: Cross-Validation

In order to validate the model and to measure the prediction performance, a cross-validation is performed. The aim of this work is to find an optimal compromise between experimental effort (size of the training data set known to the model) and prediction performance. Therefore, a manual cross-validation was applied in a structured hierarchical manner in which different calibration methods were compared on the basis of the mean absolute percentage error (*MAPE*, see Eq. (6)) and the percentage error (*PE*, see Eq. (7)) to measure the prediction performance. The calibration methods differ in the size and selection of the training data set and in the selection and number of the dependent variables. Whereby the different training data sets result from the selection and number of the independent variables.

$$MAPE = \frac{1}{N_j} \sum_i^{N_j} \left| \frac{\vec{Y}_i - f_{\text{model}}(\vec{\beta}, \vec{X}_i)}{\vec{Y}_i} \right| 100 \% \quad (6)$$

$$= \frac{1}{N_j} \sum_i^{N_j} |PE| \quad (7)$$

Where N_j is a set of experiments included in the calculation. A calibration method encompasses four components. First, which dependent variables \vec{Y} are included, second

to fourth, which measurement positions z , gas fluxes j_d and bubble column height h_c are included in the training data set. The selection of the dependent variables is intended to investigate which of these variables is best suited for optimization. The selection and number of independent variables determines the size of the training data set on which Eq. (5) is trained. In order to distinguish between the calibration methods, a composite label system is used. The labels of the data sets that were included in the training data are defined in Tab. 1.

Table 1: Composite label system to identify a calibration method.

| Y_i | Method label - included variable | | |
|-----------------------------|--|-------------------------------|---------------------------------------|
| | H - $\bar{\alpha}_{d,i}$ | M2 - $\xi_{32,i}, \sigma_i^2$ | M3 - $\xi_{32,i}, \sigma_i^2, \omega$ |
| | M2H - $\xi_{32,i}, \sigma_i^2, \bar{\alpha}_{d,i}$ | D- $\hat{f}_{d,i}^n$ | |
| X_i | Method label - included value | | |
| $j_{d,i} / \text{cms}^{-1}$ | jd3 - (3) | jd2,3 - (2,3) | jd2,4 - (2,4) |
| | jd14 - (1,4) | jd234 - (2,3,4) | jd1234 - (1,2,3,4) |
| z_i | z1 - (high) | z2 - (middle, high) | z3 - (low, middle, high) |
| $h_{c,i}$ | hc60 - (60) | hc60 - (80) | hc100 - (100) |

The label Mz2jd234hc140 for example states that Eq. (5) was solved respectively trained based on the Sauter mean diameter and the variance of the experimental data set consisting of all measurements at $z = (80, 140)$ cm and $j_d = (2, 3, 4)$ cm s^{-1} in a 140 cm high bubble column.

Optimization of the calibration method is performed only in the water + air system. This means that data with variations in the solute and its concentration are not taken into account. It is important to note that the different calibration methods have different training data sets but are all evaluated after training, for a given simulation study, on the same test data set with the *MAPE*. The *MAPE* is always calculated using the two dependent variables Sauter mean diameter (ξ_{32}) and variance (σ^2) of the measured

BSDs. The adjusted parameters $\vec{\beta}$ of all simulations and study's can be taken from the supplementary material.

4 Results and Discussion

4.1 Evaluation of the Calibration Methods

4.1.1 Choice of the Dependent Variables

In the first study, the influence of the choice and number of dependent variables is investigated. The data set of the water + air system acquired with a bubble column height of $h_c = 140$ cm was used for that study. To shorten the notation, the label of the bubble column height is omitted. The results are shown in the Section S.3.1 in the Supplementary and are only briefly summarized here.

As expected, if the gas holdup is included as the only dependent variable in the parameter estimation (method H), a *MAPE* of $> 60\%$ is obtained. If the parameter estimation is related to two moments of the BSD (method M2), the result is a *MAPE* of 12 % in average (over j_d and z). If the gas holdup is further added to the two moments of the method M2 as a dependent variable (resulting in method M2H), the *MAPE* and the *PE* with respect to the gas holdup remains more or less the same (cf. Fig. S.1).

Including another moment to the method M2, the kurtosis (method M3), shows that the *MAPE* increases to 20 % in average (over j_d and z , cf. Fig. S.2). This finding can be attributed to the large experimental uncertainty of this quantity so that an overfitting (the model memorizes the training data set instead of generalizing it) takes place. Additionally, it is important to note that no more than two independent moments should be included in the calibration method if the underlying BSD can be described by a two-parametric distribution function, e.g. Gaussian, Log-normal or Weibull, otherwise overfitting may occur.

When complete BDS (method D) is considered for calibration, the *MAPE* becomes 26 % on average (over j_d and z) and is thus larger compared to method M2. This is due to the fact that the moments are integral and therefore averaged quantities that are less sensitive to outliers and measurement noise. If the complete BSD is used instead of the two moments for the estimation of the model parameters, there is the risk that random measurement errors are represented by the model parameters. This worsens the overall prediction performance of the model for method D compared to method M2.

In summary, as expected, the calibration of the model to integral measures alone, such as the gas holdup, is not sufficient to achieve good prediction performance of the model. Instead, information is needed that reflects the specific behavior of the dispersed phase for the given process and chemical system. The BSD, or more precisely the two moments of the BSD, provides exactly this information. In the following, only two moments (Sauter mean diameter, variance) are used as dependent variables to calculate the loss function Eq. (5).

4.1.2 Choice of the Independent Variables: Gas Flux and Vertical Position

In the second study, the influence of the choice and number of independent variables on the prediction performance is investigated. For that study, the data sets from the water + air system with a bubble column height of $h_c = 140$ cm were used and the gas flux and vertical measuring position was chosen as variable independent parameters. Again, to shorten the notation, the label of the bubble column height is omitted.

Fig. 3 shows the influence of the choice and number of independent variables of method M2 on the *MAPE*. When only one vertical position and only one gas flux are used to calibrate the model, the largest *MAPE* occurs. Obviously, the training data do not represent enough information about the system. Furthermore, it can be observed that when more vertical positions are included in the training data, there is a slight trend towards an improved prediction performance of the model (cf. Fig. 3A). However, this improvement is small.

Therefore, the authors believe that the laboratory effort associated with each additional measurement position is not justified.

In contrast, if the training data set includes at least two experiments carried out with different gas fluxes, the prediction performance increases as shown in Fig. 3B. However, when data from more than two gas flows are included in the calibration, the increase in prediction performance is small compared to the case calibrated with data obtained for two gas fluxes. Obviously, these two data sets provides enough information of the behavior of the multiphase system so that a good model fit is obtained.

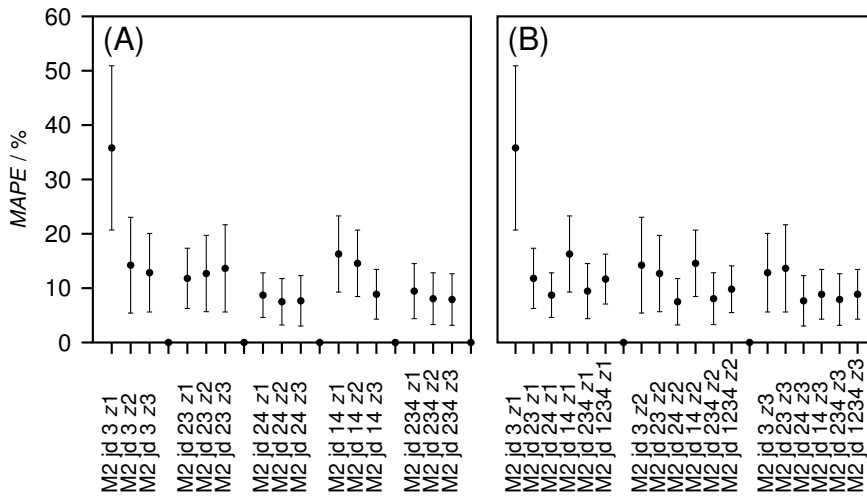


Figure 3: Mean absolute percentage error $MAPE$ (see Eq. (6)) evaluated on the water + air data set with $h_c = 140$ cm for different calibration methods (see Section 3.3.1). Grouping of the observations: (A) the number of included gas fluxes in ascending order, (B) vertical measurement position. Internal sorting of the groups: (A) the additional vertical measurement positions in ascending order, (B) gas flux and number in ascending. Evaluation data set: $h_c = 140$ cm.

It can also be observed that the $MAPE$ increases when the lowest gas flux is included in the calibration method (cf. Fig. 3B). This may be attributed to the fact that the multiphase flow is in a different flow regime under these conditions. That means that the turbulence, which influences e.g. breakage, coalescence and internal backmixing, is different compared to the experiments with higher gas flux ($j_d > 1 \text{ cm s}^{-1}$). A detailed discussion on that subject is given in Section 4.2.1.

In summary, the model can describe (interpolate) the behavior of the dispersed flow in the bubble column well for gas fluxes between $j_d = 2 \text{ cm s}^{-1}$ and $j_d = 4 \text{ cm s}^{-1}$. The

calibration method that uses two moments of the BSD (Sauter mean diameter, variance), which is measured at one vertical position only but for two different gas fluxes, is the best compromise between prediction performance of the model and experimental effort. This calibration method (M2jd24z1) is referred to in the following as the optimized calibration method.

4.1.3 Choice of the Independent Variables: Column Height

In the third and final study, the optimized calibration method (M2jd24z1) is used to investigate the influence of the choice of the bubble column height on the prediction performance. As mentioned above, the bubble column height is an independent variable that was not considered in the optimization of the calibration method. For this purpose, method M2jd24z1 is applied to various h_c and evaluated on the basis of the complete data set (all gas fluxes, measurement positions and BC heights). The Fig. 4 shows the violin plot of the percentage error PE as a function of the BC height $h_{c,cal}$ which was used as the calibration data set.

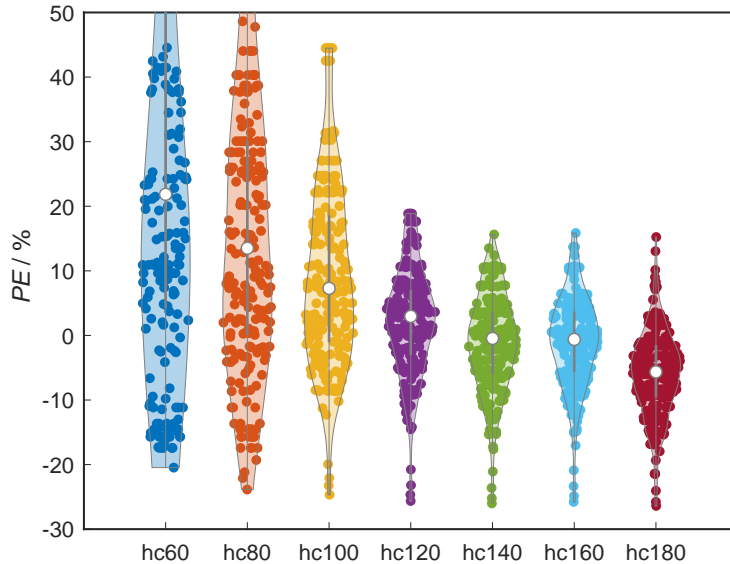


Figure 4: Violin plot of the percentage error PE as function of the BC height which was used as calibration data set. Calibration method variation hc (see Sec. 3.3.1) based on M2jd24z1. Evaluation data set: complete water + air dataset.

It can be seen that the mean value of the PE becomes smaller with increasing bubble

column height (i.e. liquid holdup), and that there are only fewer outliers. A possible explanation for this observation could be that with a small column height, the deviation from the ideal plug flow, which is assumed in the model, is expressed more strongly than with a large column. In addition, the applied measurement probe (OMOP) is invasive. That means, that the volume of the column influenced by the probe is relatively large in comparison to the total holdup of the column when the height of the column is small.

In summary, the higher the bubble column, the better the predication performance. A height of 1.4 m is considered as sufficient (cf. Fig. S.3).

4.2 Investigation of Prediction Performance

4.2.1 Bubble columns height and Gas Flux

Fig. 5 shows the Sauter mean diameter as a function of the z -direction for different BC heights (A)-(F) and gas fluxes j_d (colors). The boundary values are marked as stars. The values that are used for the calibration are marked by a crosshair (see Fig. 5D). The model was calibrated using the optimized method (M2jd24z1) with the $h_c = 1.4$ m data set (see Sec. 4.1.2). Note that Fig. 5 corresponds to the data series measured with a bubble column height of 1.4 m shown in Fig. 4.

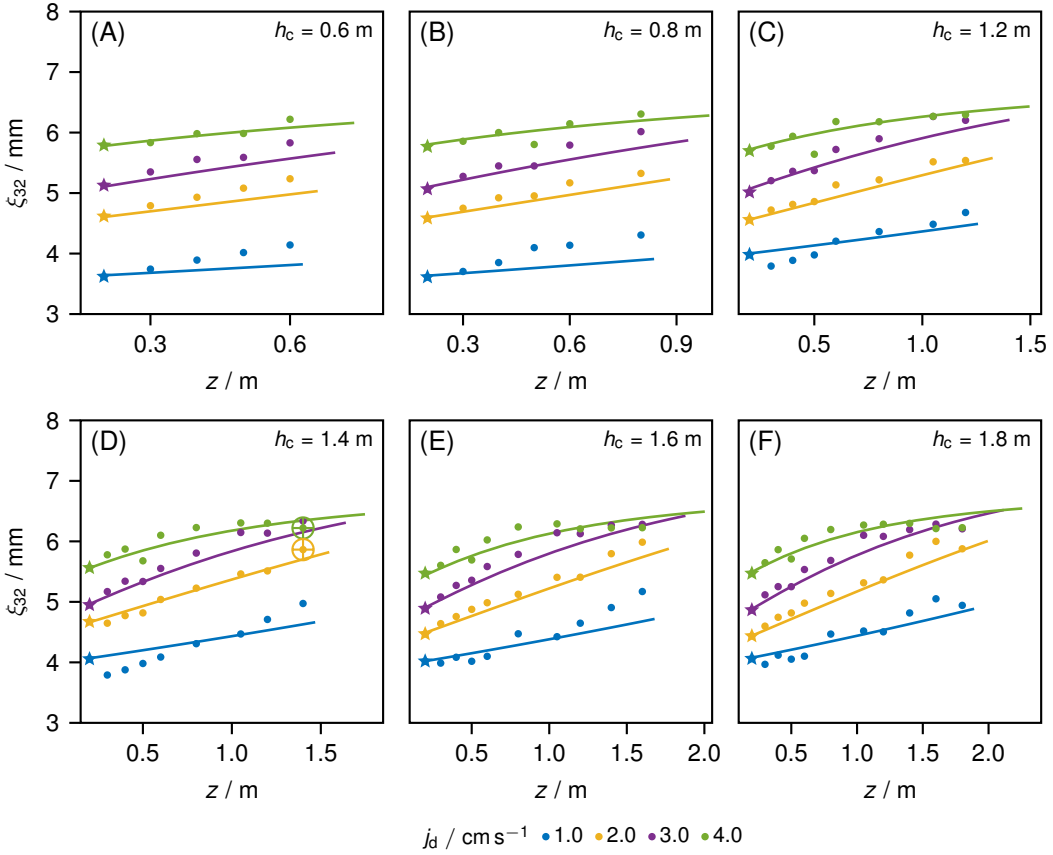


Figure 5: Sauter mean diameter ξ_{32} as a function of the z -direction for different gas fluxes j_d (color) and different bubble column heights h_c (A) to (F). Calibrated with method $Mj_d2, 4z1$ with $h_c = 1.4$ m. Definitions: Experiments (symbols), model predictions (lines), calibration points (crosshairs), boundary values (stars). Chemical system: water + air.

The experimental data reflect the expectations: the Sauter mean diameter increases with increasing vertical position and gas flux. The latter observation is mainly due to the fact that as the gas flux increases, more turbulence is introduced into the system, which in turn leads to an increased coalescence frequency. The vertical position corresponds with the residence time of the gas phase and thus the total number of coalescence events. Therefore, the bubble diameter increases with residence time and vertical position, respectively. After a certain vertical position in the column, the Sauter mean diameter no longer increases linearly. Instead, its slope decreases. This decrease in slope can be attributed to the higher breakup frequencies of larger bubbles. On the other hand, at that position the fraction of bubbles whose size is larger than the maximum bubble diameter that can be captured by the OMOP is no longer negligible.

In addition, it can be observed that the increase in Sauter mean diameter is approximately equidistant for gas fluxes $j_d = (2.0, 3.0, 4.0) \text{ cm s}^{-1}$. Between $j_d = 2.0 \text{ cm s}^{-1}$ and $j_d = 1.0 \text{ cm s}^{-1}$, however, a larger difference in Sauter mean diameter can be observed. This increase may indicate a change in the flow regime, as described above. This changes the turbulence in the column and thus the bursting and coalescence of the bubbles. Obviously, the simple turbulence model used in this work (see Sec. 3.1), which describes a linear relationship between the turbulent energy dissipation rate and the gas flow, is not able to correctly reproduce this change in the flow regime.

The comparison of experimental data and simulation results shows that the model can reliably predict the Sauter mean diameter in a wide range of process parameters (i.e. BC heights and gas fluxes). The deviation of the model measured with the *MAPE* evaluated within the respective BC height is shown in Fig. S.3 in the Supplementary. It is important to mention that only the two data, which are shown with crosshairs in the figure, were used for the calibration of the model.

Even the transformation from a linear shape at a lower BC height (cf. Fig. 5A) to a more curved shape at a higher BC height (cf. Fig. 5F) can be reproduced by the model without any prior knowledge of that behavior which indicates that the OMOP was not yet at its measurement limit as mentioned above. The largest deviations between model predictions and experimental data are found for a gas flux of $j_d = 1.0 \text{ cm s}^{-1}$.

In all likelihood, these large deviations are again caused by the change of flow regime discussed above, which obviously cannot be adequately described by the model. A different model to describe the turbulent energy dissipation rate, other than the extremely simple approach taken in this work by Baird, Rice [35] (see Eq. (S.17)), could probably improve the prediction accuracy. However, this optimization of the model was not the focus of this work and will be considered in more detail in a future work. It is important to note that despite these limitations of the model, the general trend of the dispersed flow behavior is well predicted for the low gas fluxes.

4.2.2 Chemical System

Fig. 6 shows the Sauter mean diameter as a function of concentration of solute c_s for the aqueous solutions of ethanol (A), glycerol (B) sodium chloride (C) and sodium sulfite (D) for the lowest vertical measurement position available. The gas flux was varied depending on the chemical system in the range $j_d = (1.0, \dots, 5.0) \text{ cm s}^{-1}$. For the sake of clarity, not all gas fluxes have been depicted, but are available in the supplementary material. The liquid holdup (BC height) was constant at $h_c = 180 \text{ cm}$ during these measurements.

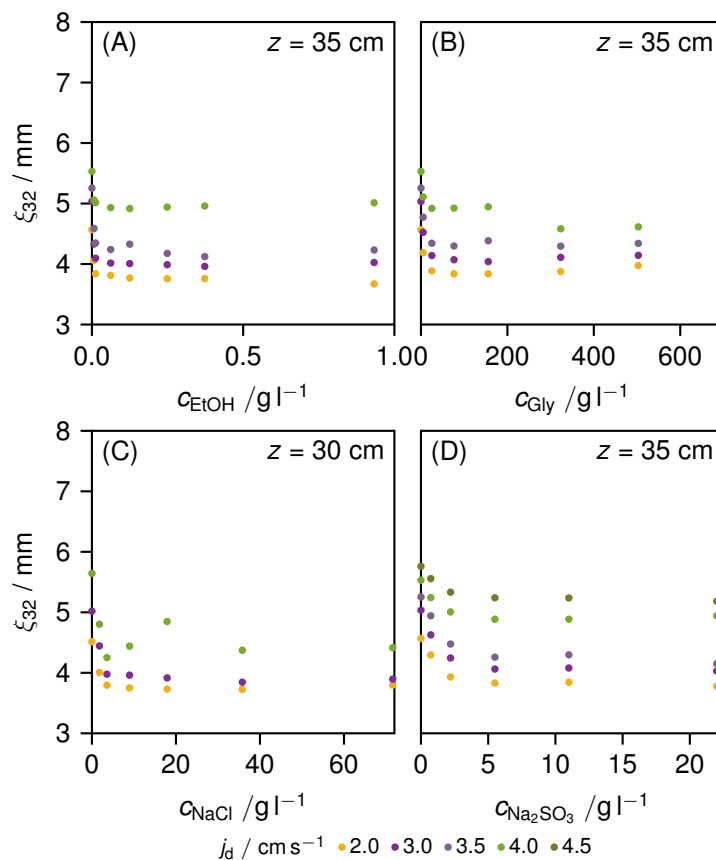


Figure 6: Sauter mean diameter ξ_{32} as a function of the solute concentration c_s for different aqueous mixtures for different superficial gas velocity j_d (color) at the lowest available measuring position z . Solutes: ethanol (A), glycerol (B) sodium chloride (C) and sodium sulfite (D).

Fig. 6 shows that regardless of the chemical system, the Sauter mean diameter initially decreases with increasing concentration and then remains almost constant. This form of the curve indicates that the addition of the solutes inhibits coalescence of bubbles. Similar observations are reported in other works, e.g. [33, 37–40].

The aqueous mixtures with glycerol show a somewhat different behavior than the other mixtures. First the Sauter mean diameter decreases but it begins to increase again at higher concentrations of glycerol. This behavior was also found by Samaras et al. [40] and is attributed by the author to the influence of the viscosity of the liquid phase.

The comparison between experimental data and model prediction for the different aqueous solutions is summarized in Fig. 7. It shows the Sauter mean diameter as a function of the z -direction for differently concentrated aqueous solutions of glycerol (A)-(D), sodium chloride (E)-(H), sodium sulfite (I)-(L) and ethanol (M)-(P). In addition, the gas flux was varied for each system. The calibration was performed only once for each chemical system with the optimized calibration method (i.e. one distinct concentration of solute, two gas fluxes and one additional vertical position). This data set is marked with a crosshair in the figure.

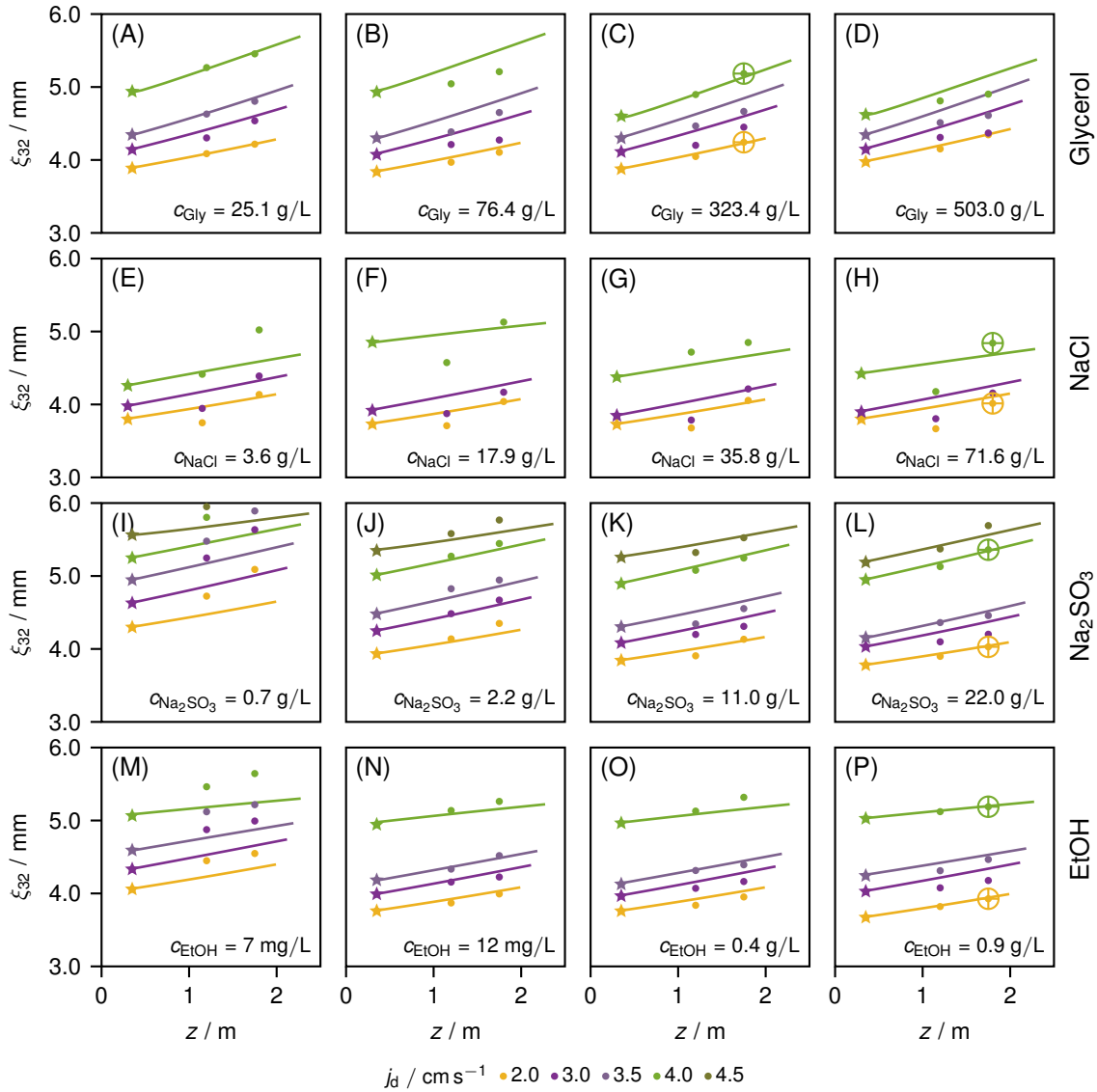


Figure 7: Sauter diameter ξ_{32} as a function of the z -direction for different gas fluxes j_d (color) and different aqueous mixtures of glycerol (A)-(D), sodium chloride (E)-(H), sodium sulfite (I)-(L) and ethanol (M)-(P) at different concentrations. Definitions: Experiments (symbols), simulations (lines), calibration points (crosshairs), boundary values (stars).

Fig. 7 shows that all chemical systems, including the water + air system discussed in the previous section, behave similarly as the vertical position or gas flow is increased, namely that the bubble diameter becomes larger. Furthermore, Fig. 7 shows that the model can predict the Sauter mean diameter over a wide range of concentrations of solute and gas fluxes. However, it is noticeable that the model mostly underestimates the Sauter mean diameter and that the lowest concentration of solute (farthest from the calibration point) has the lowest prediction performance.

If the fitted model parameters are directly transferred from one system (e.g. water + air) to another (e.g. aq. EtOH + air), the prediction performance of the model decreases significantly, as expected. However, the general trends are still correctly described (not shown here). Since the concentration-dependent property data (density and viscosity of the liquid phase, surface tension) vary only slightly in the investigated range, information reflecting the properties of the considered chemical system must be contained in the fitted model parameters and the inlet BSD. Thus, in order to predict the behavior of bubbles in bubble columns for any chemical system without having to measure the inlet BSD for the given system and process conditions in each case, a reliable model of bubble formation in the installed disperser is necessary. First attempts have been made by the authors with the adaptation and extension of the model suggested by Geary, Rice [41]. However, the development of a model describing the behavior of bubble formation is not in the scope of this work.

For the system aq. NaCl + air, large deviations between the measured and predicted Sauter mean diameter can be observed at a vertical measurement position of 1.2 m (see Fig. 7P to Fig. 7H). This deviation could be a measurement error or it could be a feature of the real system behavior that cannot be adequately described by the model.

To get a further impression of the prediction performance of the model, Fig. 8 shows comparison of the predicted and measured normalized number density distribution \hat{f}_d^n (see Eq. (S.46)) as a function of diameter ξ for different vertical positions z and gas fluxes j_d for the system aq. NaCl + air. The model can predict the experimental results (figures in the second and third column) well for different process parameters even though the model was calibrated using data from measurements with a different concentration of NaCl.

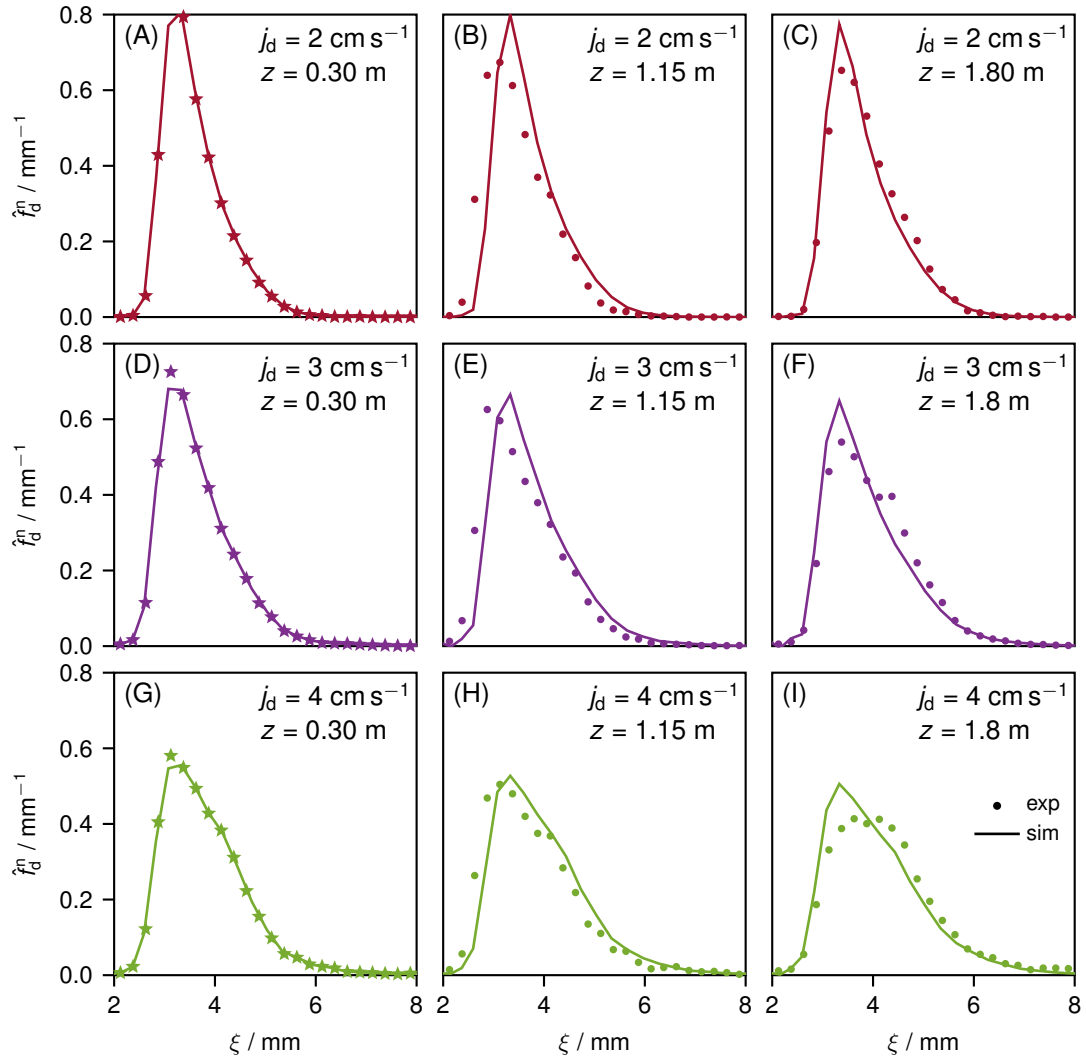


Figure 8: Normalized number density distribution \hat{f}_d^n as a function of bubble diameter ξ for different gas fluxes j_d (color, along rows) and vertical positions z . Chemical system: aq. NaCl + air ($c = 3.6 \text{ g L}^{-1}$). Simulated with the fit parameters of aq. NaCl + air ($c_{\text{NaCl}} = 71.6 \text{ g L}^{-1}$). Experiments: symbols, simulations: lines, boundary values: stars.

4.3 Scenario Test

4.3.1 Chemical System

In the first scenario, the influence of the chemical system on the local interfacial area density is investigated. Fig. 9 shows the influence of the concentration of ethanol on the profiles of the interfacial area density a , mean diameter ξ_{10} and gas volume fraction α_d .

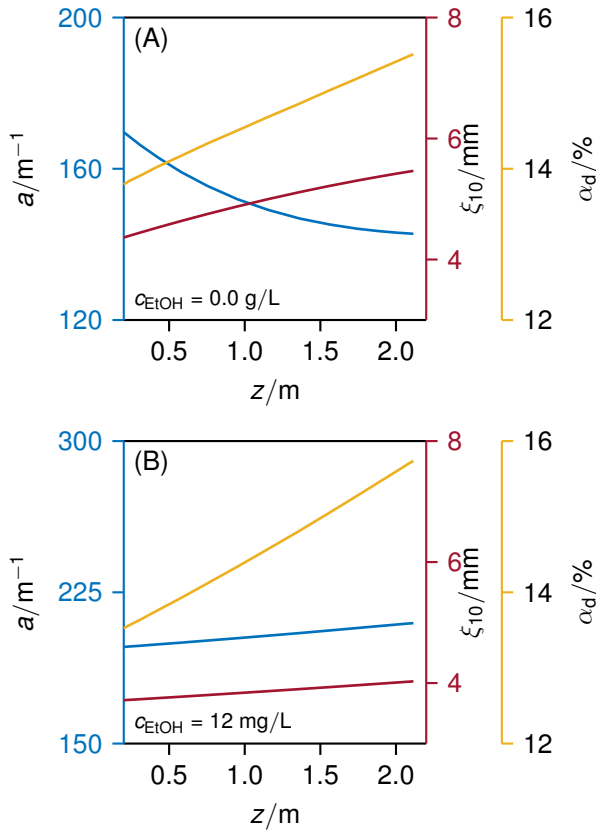


Figure 9: Interfacial area density a (blue), gas volume fraction α_d (yellow) and mean diameter ξ_{10} (red) as a function of vertical height z for (A) water and (B) aq. EtOH + air.

For both chemical systems, the gas volume fraction and the mean diameter increase as expected with the height. The interfacial area density, however, shows a complete different profile for both chemical systems. While it increases in the water system, it decreases in the system aq. EtOH + air. The different trends are caused by the complex interaction of local BSD and gas fraction. The interfacial area density has a major influence on the local mass transfer. The local gas (or liquid) fraction is important for local conversion rates or they can even influence the internal fluid dynamics (see e.g. [23]). Thus, this study shows the importance of being able to correctly predict the local properties of the dispersed flow (bubble diameter, gas fraction, gas velocity, interfacial area) in order to be able to predict local phenomena such as mass transport and reaction rates.

4.3.2 Sparger

In the second scenario, the influence of the geometry parameters of the used sparger on the behavior of the dispersed flow is investigated. Two different types of spargers are considered: a sparger that generates small bubbles (called fine sparger) and a sparger that generates large bubbles (called coarse sparger). The assumed BSDs generated by the two different spargers are depicted in Fig. 10A and Fig. 10B. At the same gas flux, the fine sparger would cause a higher pressure drop and thus higher operating costs than the coarse sparger. As an engineer, the question now arises whether these additional operating costs are compensated for by improved mass transfer (and thus e.g. higher conversion rates and space-time-yields in the bubble column). For this purpose, the engineer must be able to estimate the influence of the initial BSD on the interfacial area and thus on mass transfer. Fig. 10C and Fig. 10D shows that the model presented in this paper can do exactly this prediction.

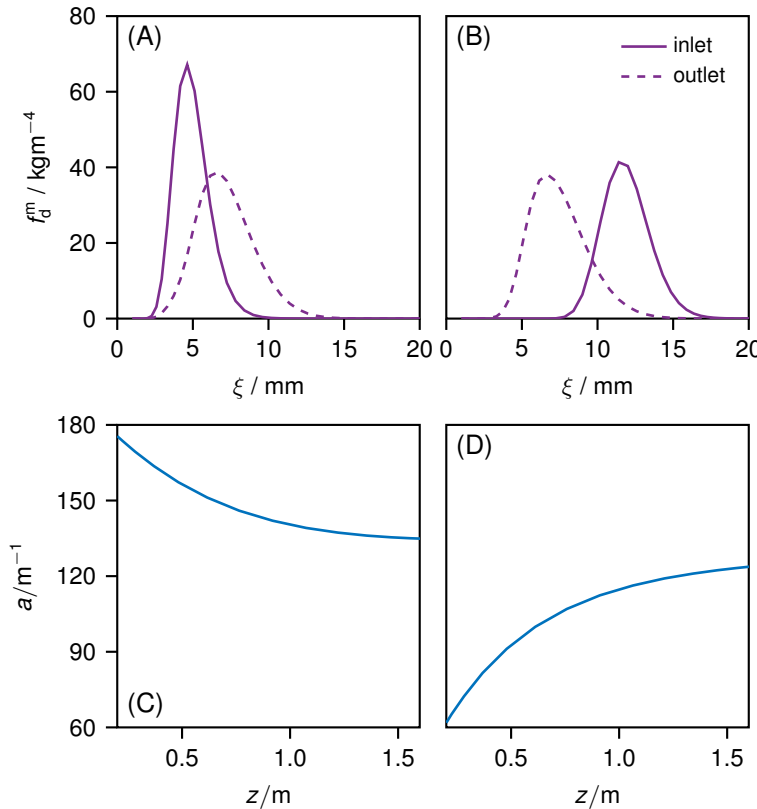


Figure 10: Mass density distribution f_d^m as a function of the bubble diameter ξ at the inlet and outlet (line style) and the interfacial area density as a function of the z -direction for the fine sparger (A,C) and coarse sparger (B,D).

Comparing Fig. 10A with Fig. 10B, it is noticeable that in the case of the fine sparger the bubbles tends to coalesce while flowing upward. In contrast, the bubbles leaving the coarse sparger break rather than coalesce. As a result, the interfacial density decreases along the column height when the fine sparger is used (cf. Fig. 10C) and it increases when the coarse sparger is used (cf. Fig. 10D). Since the growth of bubbles is negligible, both the BSD and the interface density of the two different spargers converge to similar values at the outlet of the column, due to an equilibrium of breakage and coalescence. If the model were now coupled in a next step with mass transfer and reactions in the liquid phase, a statement could be made whether the additional operating costs are worthwhile.

5 Data Availability and Reproducibility Statement

Sections 2, 3 and S.2 in this publication, along with Sections 2 to 5 of the primary source [23], provide comprehensive details on the acquisition of experimental data and application of the model. All recorded experimental data and scripts for evaluation are publicly accessible at [32]. The parameters necessary for simulation are documented in Tab. S.1 to Tab. S.4 and in the supplementary material file named *BC-Parameter.xlsx*. The numerical and experimental data corresponding to Fig. 3 - Fig. 10 are available in the supplementary material file *FigData.xlsx*, ensuring transparency and reproducibility of the study.

6 Conclusion and Outlook

In this work, a 1D multifuid population balance model approach to predict the behavior of dispersed flow in bubble columns was presented. The approach represents a compromise between computational effort and accuracy. The model enables scenarios test that can reveal the complex interaction of process parameters (e.g. gas flux), geometry parameters (e.g. column height) and properties of the chemical system.

Due to the simplifications made, it is necessary to calibrate the model to experimental data. Different calibration methods were compared in a structured hierarchical manner. An optimal calibration method could be found that minimizes the experimental effort (i.e. the number of measurements needed) while maximizing accuracy of the prediction. We found a calibration method that requires only data from one local measurement position in the bubble column acquired for two different gas fluxes. Data from approximately 600 different experiments was used to evaluate the performance of the calibration method. For this purpose, the gas flux, the bubble column height and the composition of the liquid phase were systematically varied. The calibrated model can reproduce and predict the experimental data well. Only for the smallest gas flux larger deviations were found. We assume that these larger deviations are attributable to a change in the flow regime. Obviously, the very simple turbulence model cannot adequately describe this change. Nevertheless, the model predicts the general trends correctly. To investigate the performance of the model for even larger range of parameters, more experiments in bubble columns will be carried out. Especially, the accuracy of the model predictions for larger column diameters and columns height will be of interest. Furthermore, the influence of the flow rate of the liquid phase will be studied.

To demonstrate the usefulness of the presented method, the model was applied to two scenario tests. These tests show that the model is well suited to predict the influence of process conditions and different designs on important local properties of the disperse flow, such as interfacial area density.

The presented modeling approach was applied in this work to describe disperse flow in bubble columns. In principle, even complex (three-dimensional) internal flow characteristics as they can be found for example in jet loop reactors [3] can be described by this approach. In this case, the reactor must be subdivided into characteristic compartments. Then each compartment can be described with the MPB approach. This application to more complex reactors and the inclusion of further couplings as shown in Fig. 1 is subject of future work.

Overall, it has been demonstrated that the applied 1D multifluid populations balance

approach is able to describe the general behavior of complex multiphase flow. Therefore, it is a valuable tool for engineers to get insights into the complex interactions that can occur in these systems.

Nomenclature

Latin letters

| | | |
|----------------------|---|----------------------------------|
| $a(z)$ | Interfacial area density | m^{-1} |
| $B_D(\xi, z)$ | Death rate due to bubble breakage | $\text{kg m}^{-4} \text{s}^{-1}$ |
| $B_B(\xi, z)$ | Birth rate due to bubble breakage | $\text{kg m}^{-4} \text{s}^{-1}$ |
| $C_B(\xi, z)$ | Birth rate due to bubble coalescence | $\text{kg m}^{-4} \text{s}^{-1}$ |
| $C_D(\xi, z)$ | Death rate due to bubble coalescence | $\text{kg m}^{-4} \text{s}^{-1}$ |
| c_s | Concentration of species s in the aqueous solution | kg m^{-3} |
| C_1, C_2, C_3, C_4 | Adjustable parameter of the breakage and coalescence kernel | |
| d_{BC} | Bubble column diameter | m |
| f_d^m | Mass based density function | kg m^{-4} |
| \hat{f}_d^n | Normalized number based density function | m^{-1} |
| f_{model} | Model function | - |
| f_{loss} | Loss function | - |
| g | Gravitational acceleration constant | m s^{-2} |
| h_c | ungasified liquid height, column height | m |
| $h_{c,\text{cal}}$ | h_c to which the model was calibrated | m |
| j_d | Superficial velocity of the dispersed phase, gas flux | m s^{-1} |
| $m_d(\xi, z)$ | Size dependent interfacial momentum transfer to the dispersed gas phase | $\text{kg m}^{-3} \text{s}^{-2}$ |
| $M_c(z)$ | Interfacial momentum transfer to the continuous liquid phase | N m^{-3} |
| $MAPE$ | Mean absolute percentage error (see Eq. (6)) | % |
| N_j | Set of experiments (index j) included in the calculation of the $MAPE$ | - |
| p^0 | Ambient pressure | Pa |
| $p(z)$ | Pressure | Pa |

continued ...

...continued

| | | |
|---------------|--|-------------------|
| PE | Percentage error | % |
| T^0 | Ambient temperature | K |
| $u_d(\xi, z)$ | Velocity in z -direction of the dispersed phase | m s^{-1} |
| $u_c(z)$ | Velocity in z -direction of the continuous phase | m s^{-1} |
| \vec{X} | independent variables | |
| \vec{Y} | dependent variables | |
| z | Physical coordinate along the height of the column | m |
| z_{\min} | Lower bound of the z domain | m |
| z_{\max} | Upper bound of the z domain | m |

Greek letters

| | | |
|---------------------|--|--------------------|
| $\alpha_k(z)$ | Volume fraction of the k -th phase | - |
| $\bar{\alpha}_d$ | Gas holdup | - |
| $\vec{\beta}$ | unknown parameter vector | - |
| ϵ | Termination criteria of the Picard loop | - |
| ξ | Property space coordinate representing the diameter of spherical bubbles, child bubble | m |
| $\dot{\xi}(\xi, z)$ | Growth rate | m s^{-1} |
| ξ_{\min} | Minimal bubble diameter | m |
| ξ_{\max} | Maximal bubble diameter | m |
| ξ_{32} | Sauter mean diameter | m |
| ξ_{10} | Arithmetic mean | m |
| $\rho_d(z)$ | Mass density of the dispersed phase | kg m^{-3} |
| ρ_c | Mass density of the continuous phase | kg m^{-3} |
| σ^2 | Variance | m^2 |
| ω | Kurtosis of a distribution function | - |

Subscripts

| | |
|---|-------------------------|
| B | Birth/ source term |
| c | Continuous liquid phase |

continued ...

... continued

| | |
|-----|--|
| D | Death/ sink term |
| d | Dispersed gas phase |
| i | Unique experiment identifier |
| j | Data set identifier |
| k | Phase descriptor index: d-dispersed phase, c-continuous phase |
| max | Upper bound |
| min | Lower bound |
| s | chemical species |
| sim | Simulated value |

Superscripts

| Symbol | Description |
|--------------|-----------------------|
| [^] | Normalized quantity |
| m | mass based quantity |
| n | number based quantity |

Abbreviations

| | |
|--------|--|
| aq. | aqueous |
| BC | Bubble column |
| BSD | Bubble size distribution |
| CFD | Computational fluid dynamics |
| 1D | One-dimensional |
| D | Calibration method which use the BSD as dependent variable |
| EtOH | Ethanol |
| Gly | Glycerol |
| H | Calibration method which use the gas holdup as dependent variable |
| KTAWSR | Kinetic theory approach with size resolution |
| MUSIG | Multiple-size group approach |
| MPB | 1D multifluid population balance model |
| M2 | Calibration method which use two moments of a BSDas dependent variable |

continued ...

... continued

| | |
|---------------------------------|--|
| M2H | Calibration method which use two moments of a BSD and the gas holdup as dependent variable |
| M3 | Calibration method which use three moments of a BSD as dependent variable |
| NaCl | Sodium chloride |
| Na ₂ SO ₃ | Sodium sulfite |
| OMOP | Optical multimode online probe |
| PBE | Population balance equation |

References

1. P Harriott. *Chemical Reactor Design*. CRC Press, 2002.
2. SV Patankar. *Numerical Heat Transfer and Fluid Flow*. CRC Press, 2018.
3. F Breit, O Bey, E von Harbou. Model-Based Investigation of the Interaction of Gas-Consuming Reactions and Internal Circulation Flow within Jet Loop Reactors. *Processes*. 2022; 10(7):1297.
4. LT Zhu, M Ye, ZH Luo. Application of Filtered Model for Reacting Gas–Solid Flows and Optimization in a Large-Scale Methanol-to-Olefin Fluidized-Bed Reactor. *Industrial & Engineering Chemistry Research*. 2016; 55(46):11887–11899.
5. MW Saaltink, V Vilarrasa, F de Gaspari, O Silva, J Carrera, TS Rötting. A method for incorporating equilibrium chemical reactions into multiphase flow models for CO₂ storage. *Advances in Water Resources*. 2013; 62():431–441.
6. A Brächer, LM Kreufer, S Qamar, A Seidel-morgenstern, E von Harbou. Application of quantitative inline NMR spectroscopy for investigation of a fixed-bed chromatographic reactor process. *Chemical Engineering Journal*. 2018; 336():518–530.
7. JB Joshi, VV Ranade. Computational Fluid Dynamics for Designing Process Equipment: Expectations, Current Status, and Path Forward. *Industrial & Engineering Chemistry Research*. 2003; 42(6):1115–1128.
8. CK Harris, D Roekaerts, F Rosendal, et al. Computational fluid dynamics for chemical reactor engineering. *Chemical Engineering Science*. 1996; 51(10):1569–1594.
9. R Vinuesa, SL Brunton. Enhancing computational fluid dynamics with machine learning. *Nature Computational Science*. 2022; 2(6):358–366.
10. Antony Jameson, ed. *The Present Status , Challenges , and Future Developments in Computational Fluid Dynamics*. 1995.

11. G Besagni, F Inzoli. Prediction of Bubble Size Distributions in Large-Scale Bubble Columns Using a Population Balance Model. *Computation*. 2019; 7(1):17.
12. FB Campos, P Lage. A numerical method for solving the transient multidimensional population balance equation using an Euler–Lagrange formulation. *Chemical Engineering Science*. 2003; 58(12):2725–2744.
13. D Colella, D Vinci, R Bagatin, M Masi, E Abu Bakr. A study on coalescence and breakage mechanisms in three different bubble columns. *Chemical Engineering Science*. 1999; 54(21):4767–4777.
14. C Fleischer, S Becker, G Eigenberger. Detailed modeling of the chemisorption of CO₂ into NaOH in a bubble column. *Chemical Engineering Science*. 1996; 51(10):1715–1724.
15. PL Lage. Conservation of bubble size distribution during gas reactive absorption in bubble column reactors. *Brazilian Journal of Chemical Engineering*. 1999; 16(4):339–349.
16. CP Ribeiro, PL Lage. Population balance modeling of bubble size distributions in a direct-contact evaporator using a sparger model. *Chemical Engineering Science*. 2004; 59(12):2363–2377.
17. MM Attarakih, HJ Bart, NM Faqir. Numerical solution of the bivariate population balance equation for the interacting hydrodynamics and mass transfer in liquid–liquid extraction columns. *Chemical Engineering Science*. 2006; 61(1):113–123.
18. R Gunawan, I Fusman, RD Braatz. High resolution algorithms for multidimensional population balance equations. *AICHE Journal*. 2004; 50(11):2738–2749.
19. K Sato, H Nagai, K Hasegawa, K Tomori, H Kramer, PJ Jansens. Two-dimensional population balance model with breakage of high aspect ratio crystals for batch crystallization. *Chemical Engineering Science*. 2008; 63(12):3271–3278.
20. SA Schmidt, M Simon, MM Attarakih, L Lagar G., HJ Bart. Droplet population balance modelling—hydrodynamics and mass transfer. *Chemical Engineering Science*. 2006; 61(1):246–256.
21. BH Shah, D Ramkrishna. A population balance model for mass transfer in lean liquid–liquid dispersions. *Chemical Engineering Science*. 1973; 28(2):389–399.
22. GH Yeoh, JY Tu. Population balance modelling for bubbly flows with heat and mass transfer. *Chemical Engineering Science*. 2004; 59(15):3125–3139.
23. F Breit, A Mühlbauer, E von Harbou, MW Hlawitschka, HJ Bart. A one-dimensional combined multifluid-population balance model for the simulation of batch bubble columns. *Chemical Engineering Research and Design*. 2021; 170():270–289.

24. J Solsvik, HA Jakobsen. A Combined Multifluid-Population Balance Model Applied to Dispersed Gas–Liquid Flows. *Journal of Dispersion Science and Technology*. 2014; 35(11):1611–1625.
25. CB Vik, J Solsvik, M Hillestad, HA Jakobsen. A multifluid-PBE model for simulation of mass transfer limited processes operated in bubble columns. *Computers & Chemical Engineering*. 2018; 110():115–139.
26. E Krepper, D Lucas, T Frank, HM Prasser, PJ Zwart. The inhomogeneous MUSIG model for the simulation of polydispersed flows. *Nuclear Engineering and Design*. 2008; 238(7):1690–1702.
27. M Mickler, HJ Bart. Optical Multimode Online Probe: Erfassung und Analyse von Partikelkollektiven. *Chemie Ingenieur Technik*. 2013; 85(6):901–906.
28. PK Hui, HJ Palmer. Uncatalyzed oxidation of aqueous sodium sulfite and its ability to simulate bacterial respiration. *Biotechnology and bioengineering*. 1991; 37(4):392–396.
29. A Mühlbauer, O Böck, R Raab, MW Hlawitschka, HJ Bart. Solid Particle Effects in Centi-scale Slurry Bubble Columns. *Chemie Ingenieur Technik*. 2021; 93(1-2):318–325.
30. M Lichti, J Schulz, HJ Bart. Quantification of Entrainment Using an Optical Inline Probe. *Chemie Ingenieur Technik*. 2019; 91(4):429–434.
31. J Schulz, K Schäfer, HJ Bart. Entrainment Control Using a Newly Developed Telecentric Inline Probe. *Chemie Ingenieur Technik*. 2020; 92(3):256–265.
32. M Koch, TM Dang, F Breit, E von Harbou. Experimental Investigation of the Bubble Size Distribution in a Mini Plant Batch Bubble Column With Variation of Gas Flux, Bubble Column Height and Composition of the Liquid Phase. *Zenodo*. 2023; 1().
33. G Besagni, F Inzoli. Bubble size distributions and shapes in annular gap bubble column. *Experimental Thermal and Fluid Science*. 2016; 74():27–48.
34. CA Coualaloglou, LL Tavlarides. Description of interaction processes in agitated liquid-liquid dispersions. *Chemical Engineering Science*. 1977; 32(11):1289–1297.
35. M Baird, RG Rice. Axial dispersion in large unbaffled columns. *The Chemical Engineering Journal*. 1975; 9(2):171–174.
36. J Solsvik, HA Jakobsen. Solution of the dynamic population balance equation describing breakage-coalescence systems in agitated vessels: The least-squares method. *The Canadian Journal of Chemical Engineering*. 2014; 92(2):266–287.
37. JE Botello-álvarez, SA Baz-rodríguez, R González-garcía, et al. Effect of Electrolytes in Aqueous Solution on Bubble Size in Gas–Liquid Bubble Columns. *Industrial & Engineering Chemistry Research*. 2011; 50(21):12203–12207.

38. D Pjontek, V Parisien, A Macchi. Bubble characteristics measured using a monofibre optical probe in a bubble column and freeboard region under high gas holdup conditions. *Chemical Engineering Science*. 2014; 111():153–169.
39. JJ Quinn, JM Sovechles, JA Finch, KE Waters. Critical coalescence concentration of inorganic salt solutions. *Minerals Engineering*. 2014; 58():1–6.
40. K Samaras, M Kostoglou, TD Karapantsios, P Mavros. Effect of adding glycerol and Tween 80 on gas holdup and bubble size distribution in an aerated stirred tank. *Colloids and Surfaces A: Physicochemical and Engineering Aspects*. 2014; 441():815–824.
41. NW Geary, RG Rice. Bubble size prediction for rigid and flexible spargers. *AICHE Journal*. 1991; 37(2):161–168.